Utilizing Magnetization Transfer Imaging to Investigate Tissue Remodeling in a Murine Model of Autosomal Dominant Polycystic Kidney Disease

Timothy L. Kline,[1] Maria V. Irazabal,[2] Behzad Ebrahimi,[2] Katharina Hopp,[2] Kelly N. Udoji,[1] Joshua D. Warner,[1] Panagiotis Korfiatis,[1] Prasanna K. Mishra,[3] Slobodan I. Macura,[3] Sudhakar K. Venkatesh,[1] Lilach O. Lerman,[2] Peter C. Harris,[2,3] Vicente E. Torres,[2] Bernard F. King,[1] and Bradley J. Erickson[1]*

Purpose: Noninvasive imaging techniques that quantify renal tissue composition are needed to more accurately ascertain prognosis and monitor disease progression in polycystic kidney disease (PKD). Given the success of magnetization transfer (MT) imaging to characterize various tissue remodeling pathologies, it was tested on a murine model of autosomal dominant PKD.

Methods: C57Bl/6 *Pkd1 R3277C* mice at 9, 12, and 15 months were imaged with a 16.4T MR imaging system. Images were acquired without and with RF saturation in order to calculate MT ratio (MTR) maps. Following imaging, the mice were euthanized and kidney sections were analyzed for cystic and fibrotic indices, which were compared with statistical parameters of the MTR maps.

Results: The MTR-derived mean, median, 25th percentile, skewness, and kurtosis were all closely related to indices of renal pathology, including kidney weight/body weight, cystic index, and percent of remaining parenchyma. The correlation between MTR and histology-derived cystic and fibrotic changes was $R^2 = 0.84$ and $R^2 = 0.70$, respectively.

Conclusion: MT imaging provides a new, noninvasive means of measuring tissue remodeling PKD changes and may be better suited for characterizing renal impairment compared with conventional MR techniques. **Magn Reson Med 75:1466–1473, 2016. © 2015 The Authors. Magnetic Resonance in Medicine published by Wiley Periodicals, Inc. on behalf of International Society for Magnetic Resonance.**

Key words: fibrosis; Gaussian mixture model; histology; in vivo imaging; quantitative MRI; skewness

INTRODUCTION

Between 1 in 400 and 1 in 1000 individuals are born with a genetically inherited disease known as autosomal dominant polycystic kidney disease (ADPKD) (1). The phenotype of ADPKD is characterized by the development and expansion of multiple cysts in both kidneys causing gradual destruction of healthy parenchyma (2). Throughout its course, healthy tissue is progressively lost to physical displacement/compression, apoptosis, inflammation, and fibrosis, leading to end-stage renal disease (3–5). Compensatory hypertrophy and hyperfiltration of residual nephrons initially compensates for the destruction of renal parenchyma; however, both kidneys eventually become massively enlarged, normal parenchyma is almost completely replaced by cysts surrounded by thick bands of fibrous tissue, and glomerular filtration rate declines into end-stage renal disease requiring dialysis or transplantation (6).

Radiologic imaging is essential for ADPKD diagnosis, monitoring, and outcome prediction (7). Imaging modalities such as ultrasound, CT, and MRI are used to monitor disease progression (8). Clinical studies use total kidney volume (TKV) measured by MRI as an image-based biomarker to follow the progression of ADPKD, because larger TKV has been shown to correlate with worse prognosis in ADPKD in both human (9) and murine (10) studies. However, there are challenges with using TKV as a marker of disease progression. For one, it is a simplification of the disease state and does not inform on microscopic disease processes that are involved with piecemeal destruction of healthy renal tissue. In addition, measurements of TKVs are time consuming and costly. The introduction of MR renal quantitative imaging techniques such as magnetization transfer (MT) imaging may provide solutions that could make up for the shortcomings of TKV.

MT detects a longitudinal magnetization exchange (cross-relaxation and/or chemical exchange) between observed water spins and targeted spins in tissue matrix and/or surrounding fluid (H^O, H^N, H^C) either directly or mediated by spin diffusion. Imaging of the MT effect has been successfully applied to study white matter brain diseases, particularly lesions associated with multiple sclerosis (11). MT within these lesions can be quantified by measuring the change in signal intensity with and without radiofrequency (RF) saturation, known as the MT ratio (MTR). MTR has been shown to decrease in lesion regions prior to detection by T2-weighted sequences (12).

[1]Department of Radiology, Mayo Clinic, Rochester, Minnesota, USA.

[2]Division of Nephrology and Hypertension Research, Mayo Clinic, Rochester, Minnesota, USA.

[3]Department of Biochemistry and Molecular Biology, Mayo Clinic, Rochester, Minnesota, USA.

Grant sponsor: National Institute of Diabetes and Digestive and Kidney Diseases; Grant number: 5-P30-DK090728-04 "Mayo Translational PKD Center (MTPC)"; Grant sponsor: National Institutes of Health; Grant numbers: DK104273, DK73608, F30DK098832; Grant sponsor: National Cancer Institute; Grant number: CA-160045 QIN; Grant sponsor: American Society of Nephrology Ben J. Lipps Fellowship.

*Correspondence to: Bradley J. Erickson, M.D, Ph.D., Department of Radiology, Mayo Clinic, 200 First Street SW, Rochester, MN 55905. E-mail: bje@mayo.edu

Received 9 September 2014; revised 6 February 2015; accepted 2 March 2015

DOI 10.1002/mrm.25701

Published online 13 May 2015 in Wiley Online Library (wileyonlinelibrary.com).

Because the microscopic changes of ADPKD involve fibrosis and tiny microscopic cysts too small to visualize on traditional MR, it is possible that MT may help in providing earlier information for disease prognosis and measuring progression. With respect to the relative MTR signal intensities of different tissues, lower MTR in cystic tissue (13) and higher MTR in fibrotic tissue (14) compared with normal healthy tissue have been reported. Histogram analysis of MTR (mean, mode, normalized peak height) has been applied to study differences in brain gray matter in multiple sclerosis (15) with MTR peak height being shown to positively correlate with brain parenchymal volume, and inversely correlate to cerebrospinal fluid volume (16). Recent renal imaging studies by Ebrahimi et al (17) found that off-resonance MT may differentiate highly fibrotic tissue from nonfibrotic tissue using a mouse model of renal artery stenosis. MT imaging has also been shown to have superior contrast compared with T2-weighted imaging for delineation of fibrous kidney tissue from surrounding fatty tissue (18). In a recent clinical study, an inverse correlation between estimated glomerular filtration rate and MTR values within the renal cortex was found (19).

Although MTR has been used to study other pathologies, its ability to provide quantitative information regarding tissue remodeling in ADPKD is unknown. In addition, renal tissue classification using MT has previously been mostly qualitative. The purpose of this study was to investigate the use of MT imaging for probing renal tissue changes in order to develop new image-based biomarkers for PKD. A mouse model that closely mirrors ADPKD in humans both genetically and phenotypically has been used (20). This model allowed direct comparison with a reference standard of histological sections in which both cystic and fibrotic tissue could be measured and compared with noninvasive MT imaging and MTR parameters.

METHODS

Mouse Model of ADPKD

The mouse model used in this study, *Pkd1* R3277C, mimicked a human mutation found homozygously or in trans with a fully inactivating allele in patients with typical ADPKD or in utero onset disease, respectively (21,22). The mutation lowers the level of the functional *PKD1* gene product below a critical threshold for cystogenesis (20). Mice homozygous for the allele $Pkd1^{R3277C/R3277C}$ ($Pkd1^{RC/RC}$) develop gradual cystic disease mimicking the histological features of human ADPKD. Starting at 9 months of age, $Pkd1^{RC/RC}$ mice develop a decline in renal function as measured by blood urea nitrogen levels and have a highly significant increase in cystic and fibrotic burden as measured by histomorphometric parameters, as well as TKV represented by percent kidney weight/body weight (KW/BW) ratio (20,23). Therefore, we evaluated the correspondence of MT imaging to disease progression by imaging 22 C57Bl/6 $Pkd1^{RC/RC}$ mice at 9 (n = 3 female; n = 3 male), 12 (n = 4 female; n = 4 male), and 15 (n = 4 female; n = 4 male) months of age.

Animal Protocol

This study was reviewed and approved by the Institutional Animal Care and Use Committee of Mayo Clinic in Rochester, Minnesota, USA. Animals were handled in accordance with the National Institutes of Health guidelines on the use of laboratory animals.

Each animal was scanned at a single time point. After scanning was complete, the animals were euthanized by carbon dioxide inhalation and weighed. Cardiac puncture was performed to collect blood for blood urea nitrogen analysis. Both kidneys were then extracted, and KW was measured. The left kidney was flash frozen for potential additional analysis, whereas the right kidney was placed into a preweighed vial containing 4% formaldehyde in phosphate buffer (pH of 7.4) and paraffin-embedded for subsequent histopathological analysis. One animal had asymmetric PKD, therefore the more cystic left kidney was chosen for histological analysis and comparison with MT imaging.

MR Imaging

MR imaging was performed with an Avance DRX 700WB (Bruker BioSpin, Billerica, Massachusetts, USA) spectrometer. The unit is equipped with a 16.4 T vertical wide bore magnet and a 38-mm-diameter RF coil. Mice were anesthetized in a chamber using 3% isoflurane and then transferred to the coil's animal holder. Anesthesia was maintained throughout the scan with a flow of 1.5%–2.0% isoflurane. A control monitoring and gating system (Model 1030; SA Instruments Inc., Stony Brook, New York, USA) was used for respiratory monitoring of the signal generated by a balloon sensor. Body temperature was assessed throughout the entire session using a rectal sensor and maintained at 37°C through control of both airflow and a heating element.

Scout images were obtained in three planes (axial, coronal, and sagittal) to locate the kidneys and prescribe the subsequent sequences. For MT imaging, a fast low angle shot sequence with repetition time/echo time = 362/2.4 ms, flip angle = 15°, acquisition data size = 128 × 96, and matrix size = 256 × 128 was used to acquire two sets of images, one with and the other without RF saturation. The RF saturation pulse was applied at a 2-kHz offset (downfield from water signal) as a series of 20 Gaussian pulses, 4 ms in width, with pulse power of 15 μT, pulse bandwidth of 685 Hz, and a total irradiation time of 80.7 ms. The reconstructed voxel size was 100 × 200 μm, and four contiguous slices (each 1 mm thick) were obtained in all cases.

Histopathology

Kidneys were fixed in 4% paraformaldehyde and stained with H&E for determination of cystic index. For each mouse, axial sections were sliced at the level of the renal hilum that corresponded with the prescribed axial MR slices. In addition, both Masson's trichrome and picrosirius red staining was performed to quantify the fibrotic index of each kidney specimen. Images of the stained sections were made with a Nikon SMZ800 microscope controlled through the NIS-Elements software package (Nikon Instruments Inc., Melville, New York, USA).

Table 1
Basic Measurements for the 22 C57Bl/6 *Pkd1*$^{RC/RC}$ Mice

	9 Months Old		12 Months Old		15 Months Old	
Measurement	Female	Male	Female	Male	Female	Male
Body weight, g	23.8 ± 0.4	25.8 ± 1.8	24.1 ± 1.5	29.5 ± 2.0	23.9 ± 1.5	28.5 ± 2.0
Kidney weight, g	0.9 ± 0.2	0.6 ± 0.1	1.0 ± 0.2	0.7 ± 0.1	1.0 ± 0.3	0.7 ± 0.1
KW/BW, %	3.8 ± 0.7	2.2 ± 0.2	4.0 ± 0.9	2.2 ± 0.2	4.3 ± 1.0	2.5 ± 0.3
BUN, mg/dl	45 ± 19	18 ± 3	74 ± 36	21 ± 4	93 ± 28	28 ± 3
H&E cystic index, %	22 ± 5	8 ± 3	42 ± 12	11 ± 5	42 ± 11	16 ± 9
PSR fibrotic index, %	17 ± 6	2 ± 1	16 ± 7	5 ± 1	16 ± 6	6 ± 8
TRI fibrotic index, %	18 ± 6	2 ± 1	14 ± 5	8 ± 3	18 ± 4	9 ± 10

Data are presented as the mean ± standard deviation. Cystic index was measured in H&E stained histological sections, and fibrotic index was measured by both picrosirius red and Masson's trichrome stained histological sections.
Abbreviations: BUN, blood urea nitrogen; H&E, hematoxylin and eosin; KW/BW, kidney weight/body weight; PSR, picrosirius red; TRI, Masson's trichrome.

Subsequent measurement of cystic index was quantified by color thresholding, as performed by the Meta-Morph software (Universal Imaging, Sunnyvale, California, USA). Measurements of cystic index were performed both globally and on local 1-mm^2 subregions and are reported as the percent of cysts within the total measurement area. Anatomical landmarks (eg, kidney border, macroscopic cysts, renal pelvis, etc) were used for visual coregistration between histology and MT images, with a total of 33 local measurements being made in total across the 22 mice. These regions were chosen as random samples with the goal of having a wide range of cystic index values to compare with the MTR signal. The measurement of fibrotic index was made by color thresholding with ImageJ (National Institutes of Health, Bethesda, Maryland, USA) and is reported as the percent of fibrotic tissue within the total measurement area.

Tissue Classification

MR images were transferred to a local workstation for subsequent image analysis. MTR maps were calculated as

$$\mathrm{MTR}(x,y,z) = \frac{M_0(x,y,z) - M_s(x,y,z)}{M_0(x,y,z)} = 1 - \frac{M_s(x,y,z)}{M_0(x,y,z)}, \quad [1]$$

where M_0 is the reconstructed image signal intensity obtained without saturation and M_s is the intensity obtained after RF saturation. The MTR map was computed in a voxel-by-voxel fashion. Statistical measurements of the distribution of MTR values within the kidneys were calculated and compared with the tissue indices found by histology. Both Pearson's correlation (which tests for closeness of a linear relationship between variables) and Spearman's rank correlation (which tests for closeness of a monotonic relationship) were calculated for all cases.

It has been shown that cystic tissue causes a decrease in MTR signal, whereas fibrotic tissue causes an increase in MTR signal. In addition to the statistical measurements, a Gaussian mixture model (GMM) (24) approach was used to distinguish different tissues within the kidneys as observed in the MT images. A Gaussian mixture model is a weighted sum of Gaussian densities as given by the equation

$$p(\boldsymbol{x}|\lambda) = \Sigma_{i=1}^{M} \omega_i g(\boldsymbol{x}|\mu_i, \Sigma_i), \quad [2]$$

where $\boldsymbol{x}$ is the data vector, ω_i are the mixture weights, and $g(\boldsymbol{x}|\mu_i, \Sigma_i)$ are the component Gaussian densities. Maximum likelihood estimation was then used to estimate the parameters of the GMM. After parameter estimation, probability maps were created that contain the mixing proportions of each voxel (ie, the percent of each voxel corresponding to each tissue class). Ideally, a three-tissue-class GMM approach would be used, however due to fibrotic tissue making up a very small portion of the kidney in the majority of cases, a 2 tissue-class GMM approach was used to first distinguish cystic tissue, and then fibrotic tissue was estimated from the skewness of the remaining tissue composed of both healthy parenchyma and fibrotic tissue (referred to as P-F tissue distribution). This separates the distribution of MTR values into the cystic component and a component composed of both healthy parenchyma and fibrotic tissue. Therefore, cystic index can be quantified as the ratio of the cystic component area to the total area. In addition, the subresolution fibrotic tissue causes a right-handed skewness on the parenchyma tissue class due to partial volume effects. The skewness (γ) of the P-F tissue distribution was calculated as

$$\gamma = \Sigma_{i=1}^{n} \left(\frac{\mathrm{MTR}_i - \mu}{\sigma} \right)^3, \quad [3]$$

where μ is the mean and σ is the standard deviation. The calculation was taken over all MTR values within the P-F tissue distribution (1 to n). We developed a program using Python (Python: v.2.7.4, numpy: v.1.8.1, scipy: v.0.13.3, scikit-learn: v.0.14.1) to perform analysis of the MT images.

RESULTS

A wide range of disease severity was observed in the MT images and confirmed histologically. This allowed us to study the corresponding MTR maps for a wide range of disease, from early to late stages. Table 1 lists basic measurements for the 22 C57Bl/6 *Pkd1*$^{RC/RC}$ mice grouped by age and sex. Figure 1 shows sample MT images of our ADPKD murine model specimens. The images with RF saturation on (M_s) and off (M_0), as well as the MTR maps, are shown for three example cases. Statistical measurements of MTR are given in Table 2. The MTR-derived mean, median, 25th

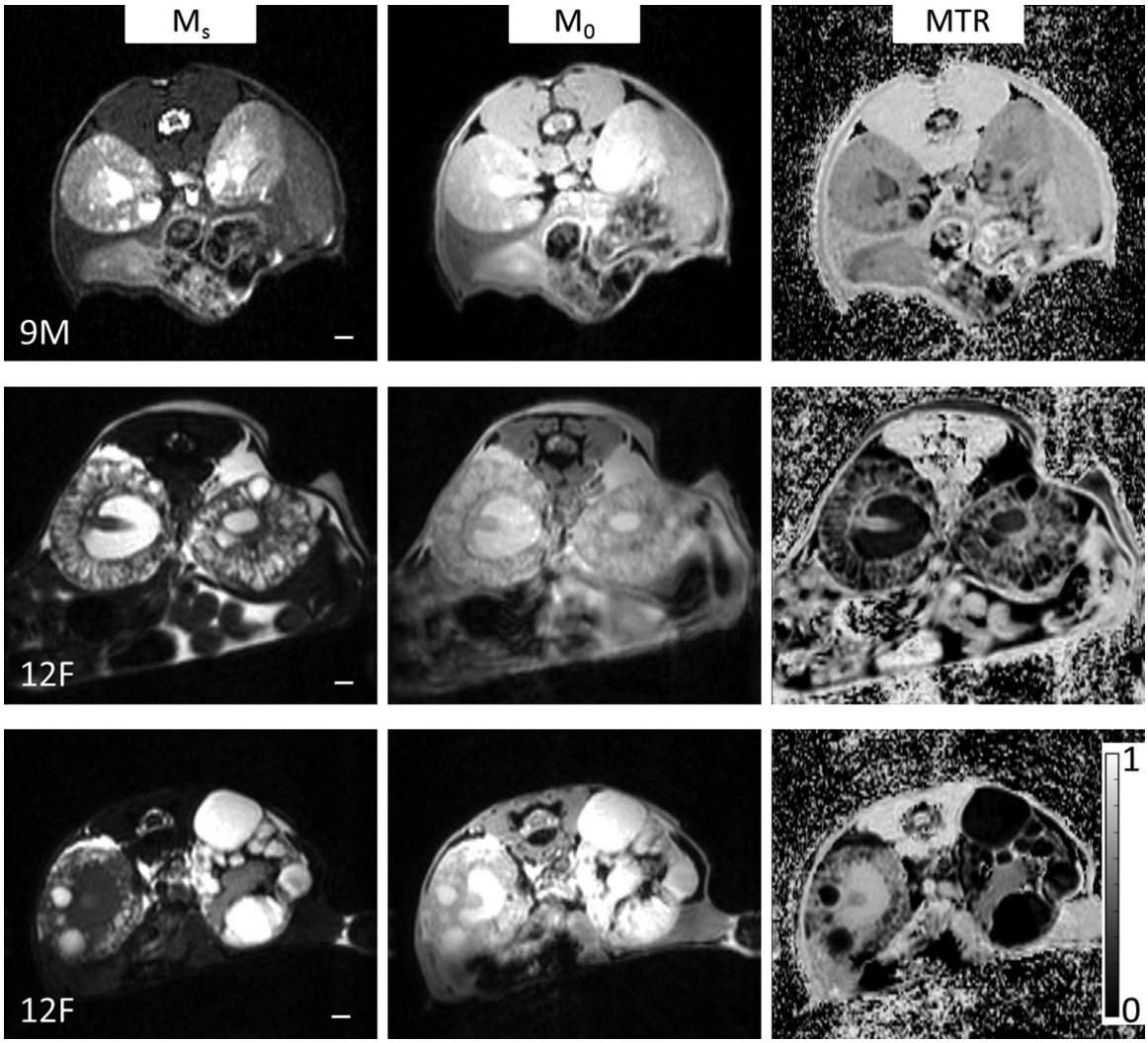

FIG. 1. Examples of three different specimens imaged by MRI. Left column: MT images obtained with saturation on (M_s). Middle column: MT images obtained with saturation off (M_0). Right column: Calculated MTR maps (computed as defined by Equation [1]). The three examples were chosen to highlight the wide range of observed phenotype expression in the mouse model. The top row highlights a fairly mild presentation of the disease in a 9-month-old male (KW/BW = 2.2%, cystic index = 5%, fibrotic index = 2%) that had a number of microcysts and a few large exophytic cysts. The middle row shows a much more severe presentation in a 12-month-old female (KW/BW = 4.3%, cystic index = 43%, fibrotic index = 10%). The bottom row shows asymmetric presentation in a 12-month-old female in which the left kidney presented much more severely than the right kidney (KW/BW = 5.3%, cystic index = 57%, fibrotic index = 9%). A color bar for the MTR images is displayed at bottom right. Scale bar = 1 mm.

percentile, and 75th percentile all decreased with age in both the female and male groups. Skewness consistently increased with age for both groups.

We found that MTR values were well correlated with cystic index. Global measurements were compared in all 22 cases. Figure 2A shows the global measurement

Table 2
Basic Statistical Measurements for the MTR Values Found Within the Mouse Kidneys

	9 Months Old		12 Months Old		15 Months Old	
Measurement	Female	Male	Female	Female	Male	Female
Mean	0.51 ± 0.06	0.57 ± 0.06	0.37 ± 0.10	0.57 ± 0.07	0.30 ± 0.05	0.49 ± 0.07
Median	0.53 ± 0.06	0.61 ± 0.05	0.37 ± 0.13	0.61 ± 0.04	0.27 ± 0.14	0.48 ± 0.08
Variance	0.018 ± 0.002	0.020 ± 0.011	0.084 ± 0.107	0.020 ± 0.024	0.034 ± 0.010	0.019 ± 0.012
25th Percentile	0.44 ± 0.06	0.57 ± 0.03	0.27 ± 0.12	0.55 ± 0.04	0.14 ± 0.10	0.40 ± 0.12
75th Percentile	0.59 ± 0.05	0.67 ± 0.02	0.54 ± 0.07	0.65 ± 0.01	0.41 ± 0.11	0.55 ± 0.06
Median absolute deviation	0.07 ± 0.01	0.04 ± 0.01	0.14 ± 0.05	0.05 ± 0.01	0.12 ± 0.05	0.08 ± 0.03
Skewness	−1.13 ± 0.50	−2.44 ± 0.17	−0.30 ± 0.57	−2.07 ± 0.35	0.23 ± 0.71	−1.06 ± 0.55
Kurtosis	2.24 ± 1.50	7.92 ± 1.20	−0.34 ± 0.73	5.27 ± 2.36	−0.19 ± 0.91	2.81 ± 0.33

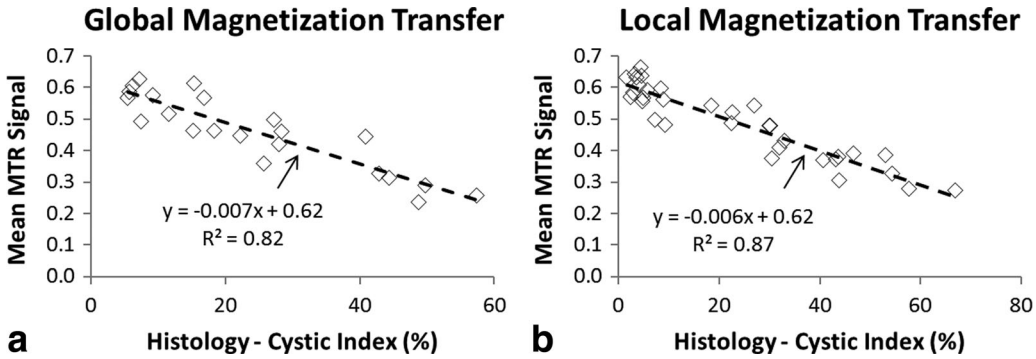

FIG. 2. **A:** Comparison of global measurement of mean kidney MTR values with the cystic index measured by histology. Although the mean MTR values are only a crude representation of the wealth of information contained in the MTR maps, the fact that they correlated closely with the cystic burden of the kidneys suggests that deeper probing can reliably extract not only macroscopic presentations of the disease but also subresolution tissue changes. **B:** Comparison of local measurement of mean kidney MTR values with the cystic index measured by histology. In this case, a much closer correlation between the results obtained by MT imaging and the ground truth histological measurements were obtained. Thus, at the local level, MT imaging conveys information regarding subresolution microscopic cysts.

comparisons of the mean MTR signal and the cystic index as measured by histology. Increasing cystic index caused a decrease in overall MTR with linear least squares regression yielding a slope of -0.007, $R^2 = 0.82$, and $P \ll 0.01$. In addition, subregions were matched between MT and histology in order to compare local measurements. In the case of local measurements (Fig. 2B, 33 comparison data points), a closer correlation ($R^2 = 0.87$, and $P \ll 0.01$) was found between the mean MTR signal and cystic index.

Using the GMM approach, we were able to closely measure cystic index and correlate fibrotic index values from the MT images. The comparison between cystic indices as measured by MT imaging (using the GMM approach) versus that found by histology is presented in Figure 3A. Figure 3B shows the results of comparing the skewness of the P-F tissue distribution found in MT imaging with the fibrotic index measured by picrosirius red–stained histology images. The correlation for cystic changes ($R^2 = 0.84$, $P \ll 0.01$) and fibrotic changes ($R^2 = 0.70$, $P \ll 0.01$) was good. In addition, for specimens having a fibrotic index greater than 7%, a right-handed skewness (greater than 0) was obtained in all cases.

Finally, in relatively advanced stages of the disease, we found that a three-tissue class GMM approach could separate cystic, healthy, and fibrotic tissues. Figure 4 shows a sample MTR map (Fig. 4A) as well as the results of applying the GMM approach (Fig. 4D). The corresponding histology slides (Fig. 4E and 4F) are shown below the probability maps for cystic index (Fig. 4B) and fibrotic index (Fig. 4C).

DISCUSSION

Quantitative medical imaging techniques are emerging that have the potential to greatly assist in evaluating disease severity and disease progression in ADPKD. These new quantitative imaging techniques could significantly add to the assessment of patient prognosis and disease progression and could allow quicker judgment of the effectiveness of interventions. In this study, we introduced the use of MT imaging for quantitative assessment of two important parameters of disease progression in an

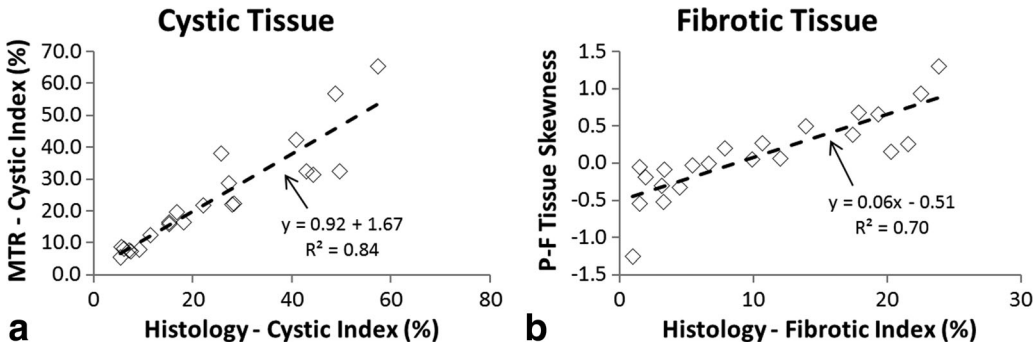

FIG. 3. **A:** Cystic index computed by the GMM approach on MTR images correlated with that measured by histology. Distinguishing the different tissues on MT by the GMM approach had very high accuracy at measuring the degree of cystic burden of each specimen. **B:** Using a two-tissue GMM approach, the skewness of the P-F tissue class was computed and correlated with the measured fibrotic index (obtained from the picrosirius red histology measurement). This correlation was very similar when compared with the Masson's trichrome–derived fibrotic index.

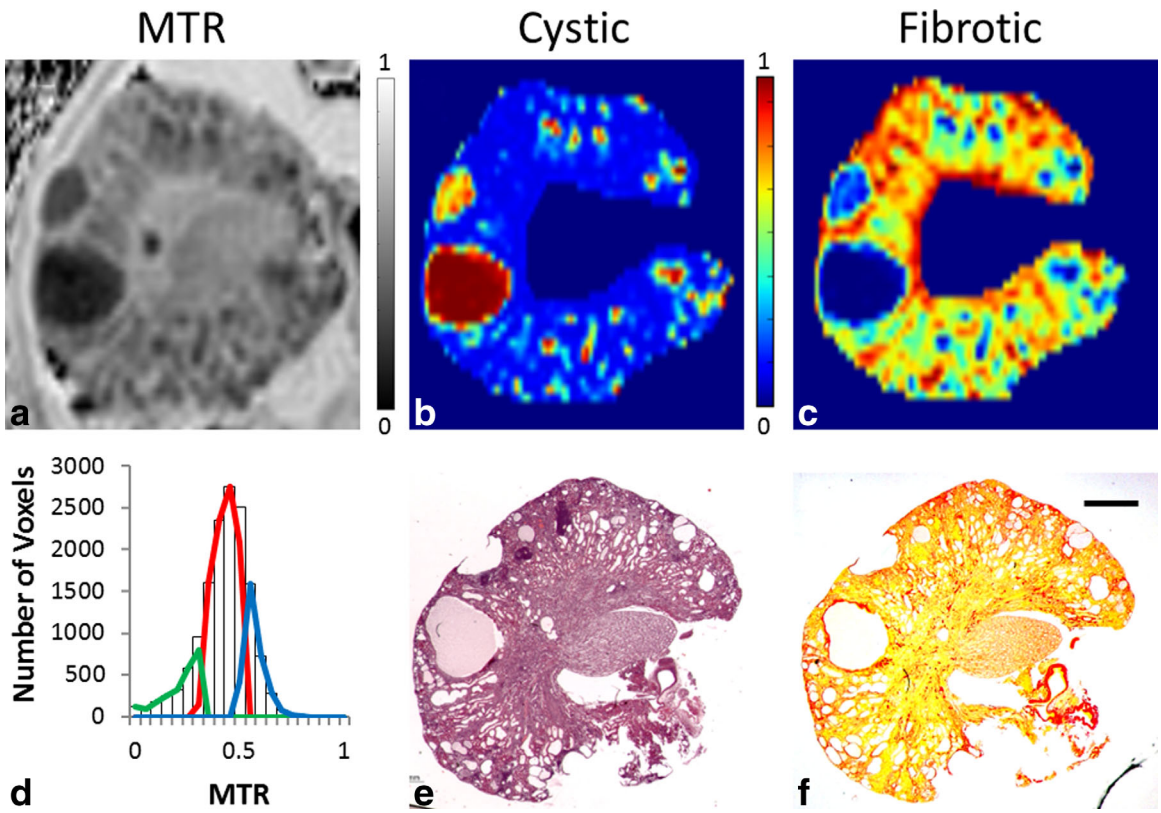

FIG. 4. **A:** MTR map. **B:** Cystic probability map displaying cystic regions in red. Microcysts (subvoxel) appear green in this representation due to voxel partial volume effects. **C:** Fibrotic probability map showing more fibrotic regions in green and red. For the corresponding panels, the color bar indicates the probability (or volume fraction) of each voxel to be cystic or fibrotic, where blue indicates 0% and red indicates 100%. **D:** MTR histogram and GMM classification overlaid. Cystic tissue is conveyed by the green component, parenchyma is conveyed by the red component, and fibrotic tissue is conveyed by the blue component. **E:** Corresponding histological slice stained with hematoxylin and eosin. **F:** Picrosirius red staining. The application of a three-tissue GMM approach to delineate both cystic (green) and fibrotic (blue) from normal healthy parenchyma tissue (red) was achievable in more severe cases such as this example (panel D). The posterior probability maps for both cysts (comparing panels B–E) and fibrotic tissue (comparing panels C–F) correspond closely to the ground truth observed in the histological slides. Scale bar = 1 mm.

animal model of ADPKD. Using a murine model of the disease, we were able to closely correlate MTR values to microscopic cystic index. In addition, we used a GMM approach to probe the presence of subresolution fibrotic tissue and extract distinct fibrotic tissue classes in more severe presentations of the disease. Because the main focus of MRI in the evaluation of ADPKD has been to measure TKV and quantify macroscopic cysts, having the ability to also probe both the presence of microscopic cysts and fibrosis would add significant benefits for both staging and better prediction of outcomes for PKD patients.

Although TKV is the gold standard for human studies, KW/BW serves as the reference standard in murine studies and is commonly used as a surrogate marker to evaluate the effectiveness of preclinical trials prior to initiating phase-1 human trials (25). When noninvasive in vivo imaging is the only option, TKV is used as a biomarker and has been shown to correlate with ADPKD progression (9). However, measurement of TKV by manual tracing of 3D MR images has been shown to be challenging (26). Importantly, however, measurement of KW has been shown to directly correlate with TKV, with an R^2 value of 0.99 (10).

There are a number of important considerations concerning the interpretation of MTR maps. The fact that healthy parenchyma tissues have MTR values in between the two types of compromised tissue critical in PKD (fibrotic and cystic) complicates analysis of the images. One can imagine an instance in which both subresolution fibrosis and subresolution cysts could have the same appearance as healthy parenchyma tissue by voxel partial volume effects. In addition, coexisting pathophysiological processes such as inflammation and edema could further complicate interpretation of MTR values in advanced cases. However, the GMM approach presented here helps to alleviate these issues. In order to probe subresolution fibrosis, the two-tissue classification method and subsequent analysis appears favorable for earlier stage classification. A distinct fibrotic tissue class would be a highly informative early stage image-based biomarker suggestive of a great deal of compromised renal tissue that has previously been unidentifiable. This could allow better evaluation of renal function, determining which patients need to be more closely monitored for their imminent need for renal replacement therapy.

There are many other quantitative imaging techniques that may also provide critical information regarding

PKD. For instance, MR diffusion-weighted imaging can extract information about both perfusion and diffusion processes within organs (27), and blood-oxygen-level-dependent imaging can measure the amount of deoxyhemoglobin present in tissues, thereby providing an estimate of renal metabolic activity (28). Other imaging techniques such as MR sodium imaging (29) and MR elastography (30) may also offer important quantitative information to better determine the status of renal tissue. Clearly, there exists a large opportunity for providing further insight into how imaging techniques can improve clinical management and treatment for PKD patients.

Although the murine model studied here closely reflects the phenotype expression seen in ADPKD patients, we observed mostly simple fluid-filled cysts, whereas in human patients, complex cysts (including calcified and hemorrhagic cysts) are often found. How these different tissues present themselves on MT requires further exploration. Also, we observed in this animal model that females have more severe disease than males, as evidenced by increased kidney weights (KW/BW ratio) and both cystic and fibrotic indices. These differences seen in the mouse model, starting at 9 months, have been discussed previously (23). Because this study considered how MTR related to renal tissue changes, these differences simply provided a wider range of disease severity for comparison purposes.

A limitation of this current study is that it did not perform longitudinal follow-up scanning of the same mouse specimens. Thus, how MT imaging relates to disease progression within the same individual is still an open question. Of particular interest will be whether MTR maps can supply critical information in the early stages of PKD that help to differentiate patients who may more quickly progress to end-stage renal disease. Having the ability to compare in vivo imaging measurements to the ground truth histological measurements (as was performed in this present study) elucidated that tissue remodeling was accurately conveyed in the MTR maps.

CONCLUSIONS

In this study, noninvasive in vivo MT imaging was used to assess tissue remodeling within a murine model of ADPKD. We found that MT imaging correlated well with both cystic and fibrotic changes within the kidneys. Therefore, MT imaging should be explored further for its ability to provide critical information regarding renal structure in renal pathologies.

ACKNOWLEDGMENTS

We thank Debra L. Hanson for help with preparation of the manuscript.

REFERENCES

1. Ecder T, Fick-Brosnahan G, Schrier RW. Polycystic kidney disease. diseases of the kidney and urinary tract. Philadelphia, PA: Lippincott Williams & Wilkins; 2006.
2. Gabow PA. Autosomal dominant polycystic kidney disease. New Engl J Med 1993;329:332–342.
3. Harris PC, Torres VE. Polycystic kidney disease. Annu Rev Med 2009;60:321–337.
4. Okada H, Ban S, Nagao S, Takahashi H, Suzuki H, Neilson EG. Progressive renal fibrosis in murine polycystic kidney disease: an immunohistochemical observation. Kidney Int 2000;58:587–597.
5. Norman J. Fibrosis and progression of autosomal dominant polycystic kidney disease (ADPKD). Biochim Biophys Acta 2011;1812:1327–1336.
6. Helal I, Fick-Brosnahan GM, Reed-Gitomer B, Schrier RW. Glomerular hyperfiltration: definitions, mechanisms and clinical implications. Nat Rev Nephrol 2012;8:293–300.
7. Bae KT, Grantham JJ. Imaging for the prognosis of autosomal dominant polycystic kidney disease. Nat Rev Nephrol 2010;6:96–106.
8. Chapman AB, Wei W. Imaging approaches to patients with polycystic kidney disease. Semin Nephrol 2011;31:237–244.
9. Grantham JJ, Torres VE, Chapman AB, et al. Volume progression in polycystic kidney disease. New Engl J Med 2006;354:2122–2130.
10. Wallace DP, Hou YP, Huang ZL, Nivens E, Savinkova L, Yamaguchi T, Bilgen M. Tracking kidney volume in mice with polycystic kidney disease by magnetic resonance imaging. Kidney Int 2008;73:778–781.
11. Dousset V, Grossman RI, Ramer KN, Schnall MD, Young LH, Gonzalez-Scarano F, Lavi E, Cohen JA. Experimental allergic encephalomyelitis and multiple sclerosis: lesion characterization with magnetization transfer imaging. Radiology 1992;182:483–491.
12. Pike GB, De Stefano N, Narayanan S, Worsley KJ, Pelletier D, Francis GS, Antel JP, Arnold DL. Multiple sclerosis: magnetization transfer MR imaging of white matter before lesion appearance on T2-weighted images. Radiology 2000;215:824–830.
13. Outwater E, Schnall MD, Braitman LE, Dinsmore BJ, Kressel HY. Magnetization transfer of hepatic lesions: evaluation of a novel contrast technique in the abdomen. Radiology 1992;182:535–540.
14. Adler J, Swanson SD, Schmiedlin-Ren P, Higgins PD, Golembeski CP, Polydorides AD, McKenna BJ, Hussain HK, Verrot TM, Zimmermann EM. Magnetization transfer helps detect intestinal fibrosis in an animal model of Crohn disease. Radiology 2011;259:127–135.
15. Ge Y, Grossman RI, Udupa JK, Babb JS, Kolson DL, McGowan JC. Magnetization transfer ratio histogram analysis of gray matter in relapsing-remitting multiple sclerosis. Am J Neuroradiol 2001;22:470–475.
16. Phillips MD, Grossman RI, Miki Y, Wei L, Kolson DL, van Buchem MA, Polansky M, McGowan JC, Udupa JK. Comparison of T2 lesion volume and magnetization transfer ratio histogram analysis and of atrophy and measures of lesion burden in patients with multiple sclerosis. Am J Neuroradiol 1998;19:1055–1060.
17. Ebrahimi B, Macura SI, Knudsen BE, Grande JP, Lerman LO. Fibrosis detection in renal artery stenosis mouse model using magnetization transfer MRI. Proc SPIE 2013;8672:867.
18. Kajander S, Kallio T, Alanen A, Komu M, Forsstrom J. Imaging end-stage kidney disease in adults. Low-field MR imaging with magnetization transfer vs. ultrasonography. Acta Radiol 2000;41:357–360.
19. Ito K, Hayashida M, Izumitani S, Fujimine T, Onishi T, Genba K. Magnetisation transfer MR imaging of the kidney: evaluation at 3.0 T in association with renal function. Eur Radiol 2013;23:2315–2319.
20. Hopp K, Ward CJ, Hommerding CJ, Nasr SH, Tuan HF, Gainullin VG, Rossetti S, Torres VE, Harris PC. Functional polycystin-1 dosage governs autosomal dominant polycystic kidney disease severity. J Clin Invest 2012;122:4257–4273.
21. Rossetti S, Kubly VJ, Consugar MB, et al. Incompletely penetrant PKD1 alleles suggest a role for gene dosage in cyst initiation in polycystic kidney disease. Kidney Int 2009;75:848–855.
22. Vujic M, Heyer CM, Ars E, et al. Incompletely penetrant PKD1 alleles mimic the renal manifestations of ARPKD. J Am Soc Nephrol 2010;21:1097–1102.
23. Hopp K, Hommerding CJ, Wang X, Ye H, Harris PC, Torres VE. Tolvaptan plus Pasireotide shows enhanced efficacy in a PKD1 model. J Am Soc Nephrol 2015;26:39–47.
24. Reynolds D. Gaussian mixture models. In: Li S, Jain A, editors. Encyclopedia of biometrics. New York, NY: Springer; 2009. p 659–663.
25. Tao Y, Kim J, Schrier RW, Edelstein CL. Rapamycin markedly slows disease progression in a rat model of polycystic kidney disease. J Am Soc Nephrol 2005;16:46–51.
26. Warner JD, Irazabal MV, Krishnamurthi G, King BF, Torres VE, Erickson BJ. Supervised segmentation of polycystic kidneys: a new application for stereology data. J Digit Imaging 2014;27:514–519.

27. Thoeny HC, De Keyzer F, Oyen RH, Peeters RR. Diffusion-weighted MR imaging of kidneys in healthy volunteers and patients with parenchymal diseases: initial experience. Radiology 2005;235:911–917.
28. Li LP, Halter S, Prasad PV. Blood oxygen level-dependent MR imaging of the kidneys. Magn Reson Imaging C 2008;16:613–625.
29. Maril N, Margalit R, Mispelter J, Degani H. Functional sodium magnetic resonance imaging of the intact rat kidney. Kid Int 2004;65: 927–935.
30. Dresner MA, Rose GH, Rossman PJ, Muthupillai R, Manduca A, Ehman RL. Magnetic resonance elastography of skeletal muscle. J Magn Reson Imaging 2001;13:269–276.